J Adv Ceram

Research Article

Achieving anti-thermal-quenching in Tb^{3+}-doped glass scintillators via dual-channel thermally enhanced energy transfer

Lianjie Li[1], Junyu Chen[1], Guanlin He[1], Xvsheng Qiao[2,3]✉, Hai Guo[1]✉

Cite this article: Li L, Chen J, He G, et al. *J Adv Ceram* 2026, **15**(1): 9221220. https://doi.org/10.26599/JAC.2025.9221220

ABSTRACT: Because of the requirements of high-temperature industrial flaw detection and oil exploration, glass scintillators for application in high-temperature X-ray imaging have attracted great interest from researchers. In this work, dual-channel thermally enhanced energy transfer (ET) is proposed to improve the thermal stability of Tb^{3+}-doped glass scintillators with excellent scintillating performance. One channel is the thermally enhanced ET from Ce^{3+} to Tb^{3+} by codoping with Ce^{3+}, and the other channel is the thermal compensation effect from traps to Tb^{3+} with increasing density of traps by codoping with Ce^{3+}. The obtained glass scintillators possess high transmittance (exceeding 86.6% at 542 nm), excellent X-ray excited luminescence (XEL) intensity (365% of that of $Bi_4Ge_3O_{12}$ (BGO)), and superior imaging resolution (24 lp/mm). In addition, anti-thermal-quenching luminescence in XEL (the XEL intensity (I_{XEL}) at 573 K is 168% of that at 303 K) is achieved. All the results undeniably demonstrated that the designed Ce^{3+} and Tb^{3+} codoped glass scintillators have significant potential for high-temperature X-ray imaging. Dual-channel thermally enhanced ET is beneficial for the development of Tb^{3+}-doped glass scintillators with superior scintillating performance and excellent thermal stability.

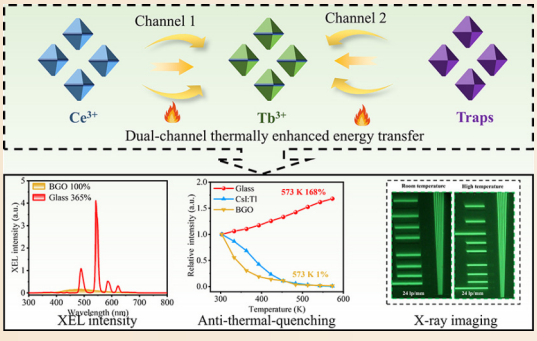

KEYWORDS: Tb^{3+}-doped glass scintillators; anti-thermal-quenching luminescence; thermally enhanced energy transfer (ET); Ce^{3+}; thermal compensation effect

1 Introduction

Scintillator materials, which can convert high-energy rays (such as X-rays and γ-rays) to low-energy visible light, are widely used in security checks, high-energy physics and medical imaging [1–4]. In high-energy physics detection and oil exploration, scintillators are exposed to high-temperature environments, which require scintillators with high thermal stability, especially anti-thermal-quenching luminescence [5–7]. However, the performance of most scintillators decreases with increasing temperature due to thermal quenching, which restricts their utility in high-temperature X-ray imaging. For example, commercial scintillators, such as CsI:Tl and $Bi_4Ge_3O_{12}$ (BGO), have difficulty maintaining scintillating performance at high temperatures [8–10]. Therefore, to meet the requirements of high-temperature applications, exploration of thermal enhancement strategies to improve the thermal stability of scintillators is urgently needed.

Glass materials are promising scintillators because of their cost-effectiveness, high transparency, compositional tunability, and ease of fabrication [5,11–14]. The chemical inertness of these materials also ensures excellent stability and corrosion resistance, making them suitable for applications in harsh environments [11–13,15]. Tb^{3+}-doped glasses are particularly attractive. The primary emission of Tb^{3+} at 542 nm, originating from the $^5D_4 \rightarrow {}^7F_5$ transition, matches well with commonly used optical charge coupling devices [16–18]. In particular, there is no cross point between the 4f ground state and the 4f excited state of Tb^{3+}, resulting in excellent thermal stability of the luminescence of Tb^{3+} [19]. However, despite the inherent stability of Tb^{3+} ions, the overall luminescence of such scintillators often degrades at high temperatures due to thermal quenching.

Several innovative strategies have been developed to suppress thermal quenching in luminescent materials. A prominent approach is to establish energy transfer (ET) pathways that compensate for thermal losses at high temperatures. These pathways generally fall into two categories. The first relies on efficient ET from sensitizers to activators. Ce^{3+} ions are usually employed as sensitizers for the activator Tb^{3+}. The strong and

[1] Department of Physics, Zhejiang Normal University, Jinhua 321004, China. [2] School of Materials Science and Engineering, Zhejiang University, Hangzhou 310027, China. [3] State Key Laboratory of Baiyunobo Rare Earth Resource Research and Comprehensive Utilization, Baotou Research Institution of Rare Earths, Baotou 014030, China.

✉ Corresponding authors. E-mail: X. Qiao, qiaoxus@zju.edu.cn; H. Guo, ghh@zjnu.cn

Received: October 9, 2025; Revised: November 11, 2025; Accepted: November 25, 2025

© The Author(s) 2026. This is an open access article under the terms of the Creative Commons Attribution 4.0 International License (CC BY 4.0, http://creativecommons.org/licenses/by/4.0/).

broadband emission of Ce^{3+}, which originates from the permissible electric dipole 5d–4f transition, renders them ideal energy donors for Tb^{3+} [20–23]. For example, the Ren and Guo groups [12] achieved zero-thermal quenching or anti-thermal-quenching by ET from Gd^{3+} to Tb^{3+} and from Ce^{3+} to Tb^{3+}, respectively. The second category involves the release of heat-stimulated carriers from traps to luminescent centers. As demonstrated by the Wu group [24], introducing suitable traps could store and subsequently release energy to the luminescent centers via a thermally enhanced process. Building on these foundations, this work proposes a "dual-channel thermally enhanced ET" strategy that synergistically combines both mechanisms. First, the thermally enhanced ET from Ce^{3+} to Tb^{3+} is realized by codoping Ce^{3+}. Second, the density of traps increases with codoping with Ce^{3+}, which enhances the thermal compensation effect from traps to Tb^{3+}. As the temperature increases, the two ET channels become increasingly efficient, delivering more energy to the Tb^{3+} activators and thereby counteracting the concurrent onset of thermal quenching.

In this work, dual-channel thermally enhanced ET, including ET from Ce^{3+} to Tb^{3+} and a thermal compensation effect from traps to Tb^{3+}, was proposed and applied to suppress the thermal quenching of Tb^{3+}. The optimal sample exhibited anti-thermal-quenching luminescence as the temperature increased from 303 to 573 K (the X-ray excited luminescence (XEL) intensity at 573 K was 168% of that at 303 K). In addition, the optimal sample presents a low detection limit (2.8 $\mu Gy_{air}/s$), impressive XEL intensity (I_{XEL}; 365% of that of BGO), and high spatial resolution (24 lp/mm). Dual-channel thermally enhanced ET has been proven to be an effective way to develop novel thermally stable Tb^{3+}-doped glass scintillators for high-temperature applications, which opens new possibilities for irradiation detection in extreme environments.

2 Experimental

2.1 Raw materials

NaF, CaF_2, Al_2O_3, SiO_2, TbF_3, CeF_3, and Al powders were used without further purification. NaF (A.R.) was purchased from Lianshi Chemical Reagent Co., Ltd., China. Al_2O_3 (A.R.) and SiO_2 (A.R.) were purchased from Sinopharm Chemical Reagent Co., Ltd., China. CaF_2 (A.R.) and Al powders (A.R.) were purchased from Zhanyun Chemical Co., Ltd., China. TbF_3 (99.99%) and CeF_3 (99.99%) were purchased from A&C Rare Earth Materials Center, China. BGO crystals with a thickness of 2 mm were purchased from the Shanghai Institute of Ceramics, Chinese Academy of Sciences, China. CsI:Tl crystals were purchased from Shanghai EPIC Crystal Co., Ltd., China. The specific parameters are listed in Table S1 in the Electronic Supplementary Material (ESM).

2.2 Synthesis of glass samples

Glasses based on $55SiO_2$–$15CaF_2$–$10NaF$–$20Al_2O_3$–$x TbF_3$–$z CeF_3$–$y Al$ (x = 0, 2, 4, 6, and 8; y = 0, 0.9, 1.0, and 1.1; z = 0.5, 0.6, and 0.7) were prepared via the traditional high-temperature melt-quenching method. These samples are labeled GL-host (x = 0; y = 0; z = 0), GL–xTb (x = 0, 2, 4, 6, and 8), GL–6Tb–yAl–0.6Ce (y = 0, 0.9, 1.0, and 1.1), and GL–6Tb–1.0Al–zCe (z = 0.5, 0.6, and 0.7). First, the raw materials were weighed accurately. Second, 15 g of raw material was mixed in an agate mortar for 40 min, and the mixture was transferred to an Al_2O_3 crucible. Third, the mixed materials were melted for 1 h (1500 °C) and poured onto a preheated copper plate (300 °C). After the samples cooled naturally to room temperature, the glasses were annealed in a muffle furnace for 4 h (400 °C). Finally, all the samples were polished to an appropriate thickness (2 mm) for subsequent investigations.

2.3 Materials characterization

X-ray diffraction (XRD) patterns were measured with an XRD (Rigaku MiniFlex/600, Rigaku, Japan). An X-ray photoelectron spectroscope (XPS; ESCLALAB 250Xi, Thermo Fisher Scientific, USA) was used to obtain spectroscopy data. A Fourier transform infrared spectrophotometer (FTIR; NEXUS 670, USA) was used to obtain FTIR spectra. The transmission spectra were obtained with an ultraviolet–visible spectrophotometer (Hitachi U-3900, Hitachi, Japan). Photoluminescence excitation (PLE) spectra, photoluminescence (PL) spectra, internal quantum efficiency (IQE), external quantum efficiency (EQE), and absorption efficiency (Abs) were measured with a spectrofluorometer (FS5 Edinburgh, UK). The refractive index (n) at 589 nm was measured via a digital refractometer (GI-RDB, Baoguang Instrument, China). The density (ρ) was measured according to Archimede's principle by using deionized water as an immersion liquid.

XEL spectra were obtained by using a spectrometer (OmniFluo960, Zolix, China). Temperature-dependent XEL spectra were measured by a fiber spectrometer (Godzilla, Shanghai TAIZI Technology Co., Ltd., China) with a copper heater. For the above measurements, the X-ray source was an X-ray tube (TUB00154-9I-W06, Moxtek, USA). The operating voltage was fixed at 30 kV. In most cases, the beam current was set at 100 μA, and the related dose rate was 21.3 mGy_{air}/s. For the measurement of variable dose rate spectra, the beam current was set in the range of 20–170 μA, and the related dose rates were in the range of 4.16–36.45 mGy_{air}/s. The X-ray images were taken by a camera (EOS 600D, Canon, Japan) with an image acquisition time of 5 s.

2.4 Molecular dynamics (MD) simulations

MD simulations were applied to emulate the structure of oxyfluoride aluminosilicate glass via the DL-POLY 2.20 package and Teter potentials modified by Du and Cormack [25,26]. The Buckingham potential is employed to model the short-range interactions between pairs of atoms. This formulation includes a repulsive term, arising from the overlap of electron clouds, and an attractive term that accounts for van der Waals (or dispersion) forces. The glass samples (GL-host and GL–6Tb–1.0Al–0.6Ce) with the composition of SiO_2–CaF_2–NaF–Al_2O_3–LaF_3 were investigated, and the numbers of atoms of GL-host and GL–6Tb–1.0Al–0.6Ce used in the MD simulations are listed in Table S2 in the ESM. Note that we used La^{3+} instead of Ce^{3+} and Tb^{3+} for the actual simulation, as La^{3+} is the most similar ion in terms of pair potential. The atoms were randomly distributed in a cubic initial simulation cell relaxed at 0 K, 0 Pa, and then the actual melt-quench process was simulated by alternately applying the canonical (nVT) and microcanonical (nVE) ensembles. The simulation bulks are heated to 6000 K and then cooled to 300 K with a nominal cooling rate of 5 K/ps. The nVT and nVE ensembles are applied during this simulated melt-quench process at each temperature step. At 300 K, the isothermal-isobaric (nPT) and nVE ensembles are used to allow the system to relax to the equilibrium volume. Visualization is performed with Visualization for Electronic and Structural Analysis (VESTA).

3 Results and discussion

3.1 Structural analysis

The distributions of Tb^{3+} and Ce^{3+} ions in oxyfluoride glass and

their effects on the glass structure are investigated via MD simulations, as shown in Figs. 1(a)–1(d). The glass structure of the GL-host (Fig. 1(a)) is mainly composed of an oxygen phase. F^- ions are dispersed in the glass host, and no significant fluoride phase separation is observed. The oxide phase shows structural features similar to those of the aluminosilicate glass network [27–29]. As shown in Fig. 1(b), $[SiO_4]$ and $[AlO_4]^-$ tetrahedra connect to each other by bridging with oxygen, forming a three-dimensional glass network. The glass modifiers Ca^{2+} and Na^+ ions are randomly distributed in the interspace as charge compensating agents.

Figure 1(c) displays the glass structure of GL–6Tb–1.0Al–0.6Ce, in which Tb^{3+} and Ce^{3+} ions are replaced by La^{3+} ions because of available La^{3+}-related charge pairwise potentials. With the introduction of LaF_3, phase separation structures of the fluoride phase are observed. Partial Ca^{2+} ions and almost all La^{3+} ions cluster together in the fluoride phase and connect with F^- ions to form irregular $[CaF_n]$ and $[LaF_n]$ ($n > 4$) polyhedral (Fig. 1(d)), respectively. Disordered $[CaF_n]$ and $[LaF_n]$ polyhedra connect to each other via shared corners, edges and faces, which have characteristics similar to those of fluoride glass [27,30,31]. It can provide a low-phonon energy environment for luminescent centers (Tb^{3+} and Ce^{3+} ions in GL–6Tb–1.0Al–0.6Ce), which reduces the probability of nonradiative relaxation and enhances the PL and scintillating performance of glasses [12]. Moreover, the surrounding aluminosilicate glass network acts as an inert protective shell for luminescent centers, which is conducive to improving the physicochemical stability of glasses.

Figure S1 in the ESM presents the XRD patterns of representative samples, including GL-host, GL–1.0Al–0.6Ce, GL–6Tb, and GL–6Tb–1.0Al–0.6Ce glasses. Figure S1 in the ESM reveals that all glasses possess an amorphous phase structure. Figure 1(e) shows the FTIR spectra of the GL-host and GL–6Tb–1.0Al–0.6Ce. Three absorption bands at 456, 714, and 1015 cm^{-1} could be observed. The absorption at 456 cm^{-1} comes from the bending vibration of the bridging oxygen of Si–O–Si and Si–O–Al [12,16,32]. The symmetrical stretching vibration of Si–O–Si and Si–O–Al between $[SiO_4]$ and $[AlO_4]^-$ tetrahedra leads to a peak at 714 cm^{-1} [16]. The peak at 1015 cm^{-1} originates from the asymmetrical Si–O–Si and Si–O–Al stretching vibration [28]. Similar absorption bands for GL-host and GL–6Tb–1.0Al–0.6Ce imply that the incorporation of TbF_3, Al powder and CeF_3 has no significant effect on the structure of the oxide phase.

Figure 1(f) shows the Raman spectra of GL-host, GL–1.0Al–0.6Ce, GL–6Tb, and GL–6Tb–1.0Al–0.6Ce. Two bands at 420–630 and 850–1170 cm^{-1} could be found among all glasses, which originated from Si–O–Si bending vibrations in the polymerized $[SiO_4]$ units and O–Si–O bending stretching in the depolymerized $[SiO_4]$ units, respectively [15]. Notably, the introduction of TbF_3 results in the emergence of a new low-frequency band at 250–400 cm^{-1}, which is attributed to the lattice modes of TbF_3 [33,34]. Crucially, the incorporation of TbF_3 creates a relatively low-photon-energy environment around the Tb^{3+} activators, as proven by the MD simulations. It suppresses nonradiative multiphoton relaxation and facilitates the high luminescent efficiency of Tb^{3+} activators.

As shown in Fig. 1(g), the transmittance of the GL-host, GL–6Tb, GL–6Tb–1.0Al–0.6Ce, and GL–6Tb–0Al–0.6Ce glasses surpassed 86.6% at 542 nm. Notably, compared with that of GL–6Tb, a pronounced redshift can be observed in GL–6Tb–0Al–0.6Ce glass with the addition of CeF_3 and without an Al reducing agent, indicating the existence of a high content of Ce^{4+} in the GL–6Tb–1.0Al–0.6Ce glass. Compared with that of GL–6Tb–0Al–0.6Ce, the absorption edge of GL–6Tb–1.0Al–0.6Ce glass blueshifted with the addition of Al powder. The blueshift is attributed to the effective reduction from Ce^{4+} to Ce^{3+}.

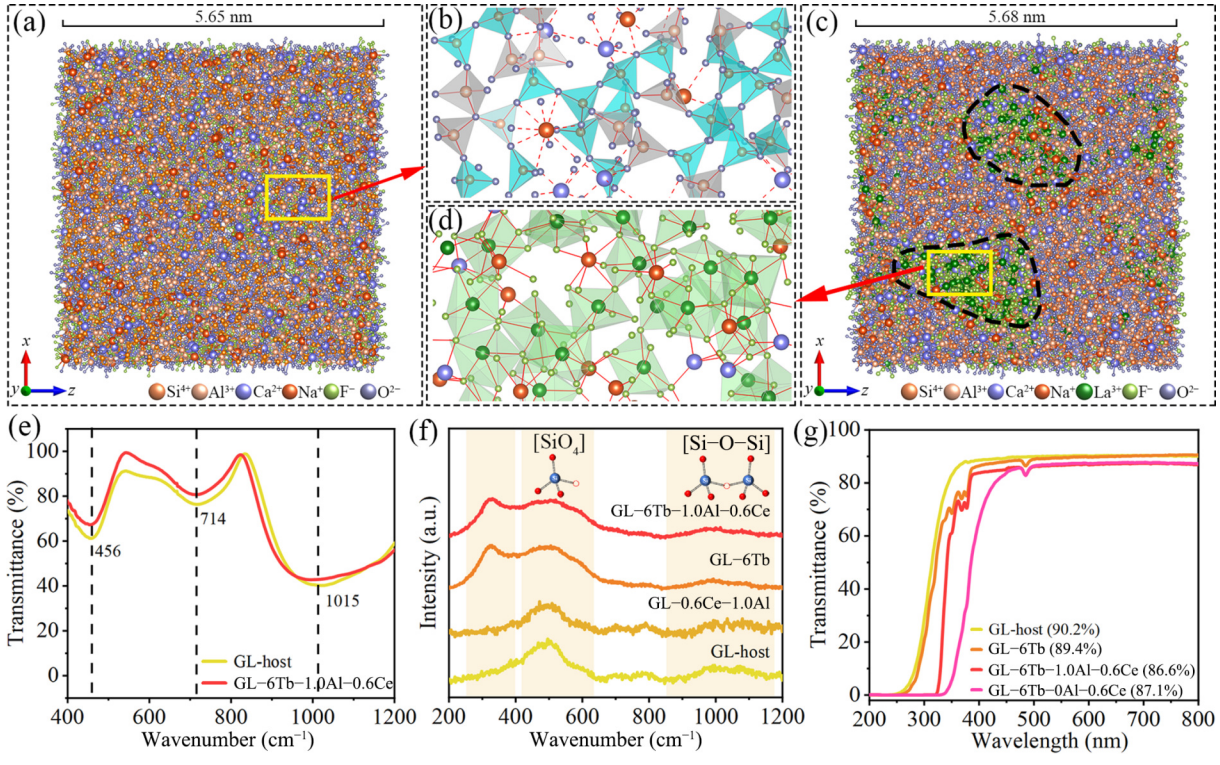

Fig. 1 MD simulations of (a) GL-host, (b) oxygen phase, (c) GL–6Tb–1.0Al–0.6Ce, and (d) fluorine phase. (e) FTIR spectra of GL-host and GL–6Tb–1.0Al. (f) Raman spectra of GL-host, GL–1.0Al–0.6Ce, GL–6Tb, and GL–6Tb–1.0Al–0.6Ce. (g) Transmittance spectra of GL-host, GL–6Tb, GL–6Tb–1.0Al–0.6Ce, and GL–6Tb–0Al–0.6Ce.

To verify this point, XPS spectra were obtained for the GL–6Tb–0Al–0.6Ce and GL–6Tb–1.0Al–0.6Ce glasses (Fig. S2 in the ESM). The content of Ce^{3+} in the GL–6Tb–0Al–0.6Ce glass is 42.9%, and it increases to 76.1% in the GL–6Tb–1.0Al–0.6Ce glass. This pronounced change confirms that the Al powder acts as an effective reducing agent, promoting the conversion of Ce^{4+} into Ce^{3+}. In addition, the energy gap (E_g) of the GL-host was calculated on the basis of transmission spectra (Fig. S3 in the ESM). The value of E_g of the GL-host is 3.90 eV, which is beneficial for the PL and scintillating performance. The refractive index, ρ, and effective atomic number (Z_{eff}) of the glass samples were also measured and are listed in Table S5 in the ESM. The incorporation of TbF_3, CeF_3, and Al clearly increased the ρ and Z_{eff} values of the glass samples, which improved their luminescent efficiency.

In summary, through MD simulations, the distributions of Tb^{3+} and Ce^{3+} ions in glass and their effects on the glass structure were theoretically analyzed. Tb^{3+} and Ce^{3+} ions are mainly distributed in the fluorine phase, which provides a low phonon energy environment; therefore, the PL and XEL intensities of glass scintillators can be increased. In addition, the introduction of the reducing agent Al can effectively reduce Ce^{4+} to Ce^{3+}, which is conducive to improving the scintillating performance.

3.2 PL properties

The optimization of the concentrations of GL–*x*Tb, GL–6Tb–0.6Ce–*y*Al, and GL–6Tb–1.0Al–*z*Ce is explored in Fig. S4 in the ESM. With increasing Tb^{3+} concentration, the PL intensity of GL–*x*Tb (x = 2, 4, 6, and 8) first increased but then decreased. The optimal sample for GL–*x*Tb is GL–6Tb. The normalized PL and PLE spectra of GL–6Tb are shown in Fig. 2(a). Under 377 nm excitation, six emission peaks at 623, 585, 542, 489, 437, and 415 nm can be detected, which originate from the transitions of $^5D_4 \rightarrow {}^7F_{3,4,5,6}$ and $^5D_3 \rightarrow {}^7F_{4,5}$ of Tb^{3+}. Monitored at 542 nm, excitation peaks at 485, 377, 368, 351, 338, 315, 300, and 283 nm and a broad band (228–278 nm) can be observed. The sharp excitation peaks stem from the transitions of $^7F_6$ to $^5D_4$, $^5D_3$, $^5L_{10}$, $^5D_2$, $^5D_1$, $^5H_7$, $^5H_6$, and $^7F_4$ of Tb^{3+}, respectively. The broad band stems from the $4f^8–4f^75d^1$ transition of Tb^{3+} [35].

To improve the luminescence of Tb^{3+}, CeF_3 was incorporated as a sensitizer. The normalized PL and PLE spectra of GL–1.0Al–0.6Ce are given in Fig. 2(b). The broad excitation band located at 321 nm originates from the 4f–5d transition of Ce^{3+}, and the broad emission band at 365 nm is attributed to the 5d–4f transition of Ce^{3+} [36]. The excitation band of Tb^{3+} at 340–380 nm and the emission of Ce^{3+} at 340–420 nm almost overlap (Fig. S5 in the ESM), which suggests the existence of ET from Ce^{3+} to Tb^{3+}. However, Ce^{3+} will be oxidized to Ce^{4+}. Ce^{4+} ions strongly absorb ultravisible (UV) light, and there is competitive absorption with Ce^{3+}. In addition, Ce^{4+} ions do not emit light under UV light excitation. A large amount of Ce^{4+} existing in glass has a negative effect on the PL performance of glasses [37]. Therefore, Al powder was introduced as a reducing agent to prevent Ce^{3+} from being oxidized to Ce^{4+}. As displayed in Figs. S4(c)–S4(f) in the ESM, the optimized contents of CeF_3 and Al are 0.6 and 1.0 mol%, respectively. The normalized PL and PLE spectra of the optimal sample GL–6Tb–1.0Al–0.6Ce are given in Fig. 2(c). When monitoring at 542 nm, the PLE spectra exhibit a broad band spanning 230–350 nm and several sharp excitation peaks. The sharp peaks are attributed to the excitation of Tb^{3+} ions. The broad band corresponds to the excitation band of Ce^{3+} because of the similar shape and position of the broad band in Fig. 2(b), which could illustrate the existence of ET from Ce^{3+} to Tb^{3+}. Under 321 nm excitation, the emission of Tb^{3+} can be detected, and reabsorption at 364–385 nm can be observed, which could further prove the ET from Ce^{3+} to Tb^{3+}.

The IQE, Abs, and EQE of GL–6Tb and GL–6Tb–1.0Al–0.6Ce are given in Fig. 2(d) and Fig. S6 in the ESM. Compared with those of GL–6Tb, the values of IQE, Abs, and EQE of GL–6Tb–1.0Al–0.6Ce are improved to 85.3%, 93.4%, and 79.7%, respectively. This enhancement indicates that the incorporation of CeF_3 could improve the luminescent efficiency of glasses.

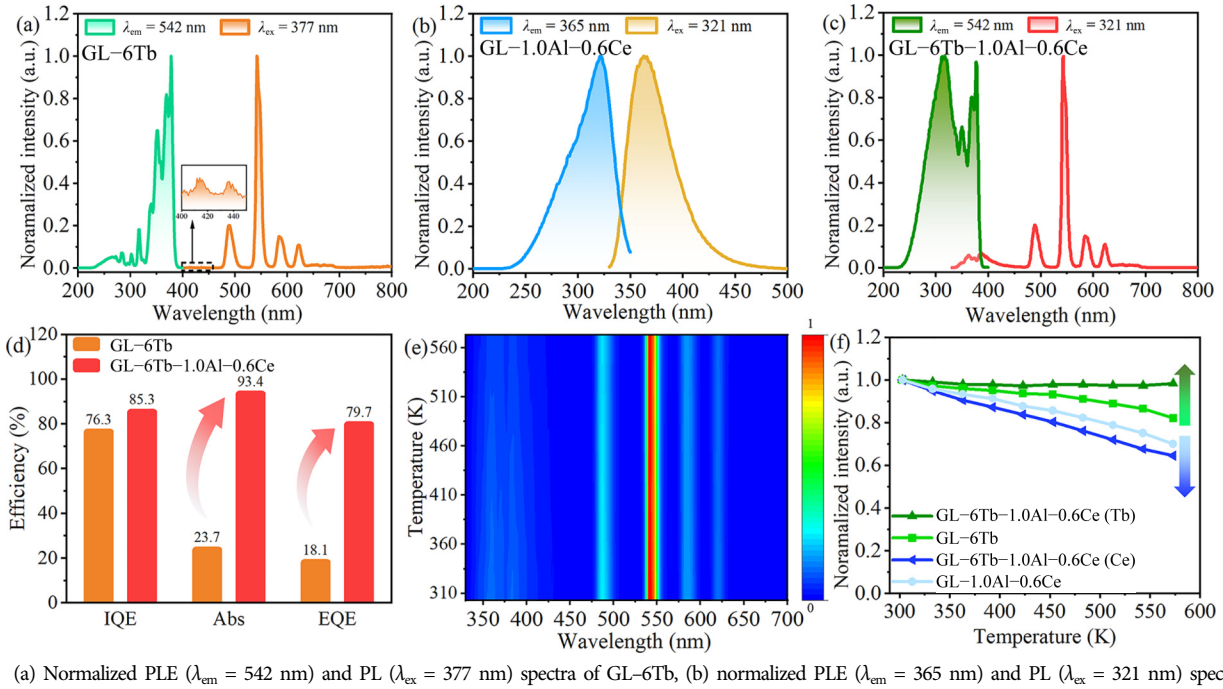

Fig. 2 (a) Normalized PLE (λ_{em} = 542 nm) and PL (λ_{ex} = 377 nm) spectra of GL–6Tb, (b) normalized PLE (λ_{em} = 365 nm) and PL (λ_{ex} = 321 nm) spectra of GL–1.0Al–0.6Ce, and (c) normalized PLE (λ_{em} = 542 nm) and PL (λ_{ex} = 321 nm) spectra of GL–6Tb–1.0Al–0.6Ce. (d) IQE, Abs, and EQE values of GL–6Tb and GL–6Tb–1.0Al–0.6Ce. (e) Contour plot of temperature-dependent PL spectra (λ_{ex} = 321 nm) of GL–6Tb–1.0Al–0.6Ce. (f) Relative PL intensity at different temperatures ranging from 303 to 573 K.

The thermal stability of the PL of the optimized GL–6Tb–1.0Al–0.6Ce glass reveals excellent performance, as shown in Fig. 2(e). The integrated PL intensity of GL–6Tb–1.0Al–0.6Ce at 573 K remains at 90.2% of its initial value at 303 K (Fig. S7(a) in the ESM). Compared with those of GL–6Tb and GL–1.0Al–0.6Ce, the PL thermal stability of GL–6Tb–1.0Al–0.6Ce significantly improved. Under the same conditions, the PL intensities of GL–6Tb and GL–1.0Al–0.6Ce at 573 K are 82.1% and 70.0% of those at 303 K, respectively (Figs. S7(b)–S7(c) in the ESM). As shown in Fig. 2(f), as the temperature increased, the thermal quenching of the Ce^{3+} emission of GL–6Tb–1.0Al–0.6Ce became more serious than that of GL–1.0Al–0.6Ce, whereas the Tb^{3+} emission of GL–6Tb–1.0Al–0.6Ce increased compared with that of GL–6Tb. The remarkable thermal stability of PL is attributed to the thermally enhanced ET process from Ce^{3+} to Tb^{3+}. This hypothesis is confirmed by the temperature-dependent decay curves (Fig. S8 in the ESM). The ET efficiency increases from 57.6% at 303 K to 63.5% at 573 K. This result proves that thermally enhanced ET effectively compensates for thermal quenching, leading to superior PL thermal stability. In addition, GL–6Tb–1.0Al–0.6Ce glass demonstrates excellent thermal cycling stability, with its PL intensity fully recovering after five consecutive heating–cooling cycles in the 303–573 K range (Fig. S9 in the ESM).

In summary, GL–6Tb–1.0Al–0.6Ce glass exhibited a 14.8-fold increase in PL (Fig. S10 in the ESM) and a high IQE of 85.3% due to the establishment of efficient ET channels from Ce^{3+} to Tb^{3+}. In addition, GL–6Tb–1.0Al–0.6Ce demonstrates remarkable PL thermal stability, with the PL intensity at 573 K retaining 90.2% of its room-temperature value because of thermally enhanced ET from Ce^{3+} to Tb^{3+}. A thermally enhanced ET channel efficiently enhances the thermal stability of the PL of Tb^{3+}.

3.3 XEL properties of GL–6Tb–1.0Alv0.6Ce

The optimization of the concentrations of GL–*x*Tb, GL–6Tb–*y*Al–0.6Ce, and GL–6Tb–1Al–*z*Ce in XEL was explored and is shown in Fig. S11 in the ESM. The optimal sample in XEL is GL–6Tb–1.0Al–0.6Ce glass. The result is in good agreement with that of the PL. The XEL properties of GL–6Tb–0.6Ce–1.0Al, including the X-ray attenuation ability, XEL intensity, irradiation hardness, and repeatability, were investigated and are displayed in Fig. 3.

Figure 3(a) compares the X-ray attenuation ability of GL–6Tb–1.0Al–0.6Ce, BGO, CsI:Tl, and CaF_2:Eu as a function of photon energy. The X-ray absorption coefficient of GL–6Tb–1.0Al–0.6Ce is comparable to that of CaF_2:Eu and slightly lower than those of BGO and CsI:Tl. When the thickness of GL–6Tb–1.0Al–0.6Ce is 2 mm, X-ray photons can be attenuated by 99.98% (Fig. 3(b)), which illustrates that GL–6Tb–1.0Al–0.6Ce has a good ability to attenuate high-energy photons.

The XEL spectra of BGO, GL–6Tb, and GL–6Tbv1.0Al–0.6Ce are given in Fig. 3(c). A significant increase in the XEL intensity is observed upon CeF_3 codoping. Specifically, the XEL intensity of GL–6Tb is 245% of that of BGO, and the XEL intensity is further improved to 365% for the GL–6Tb–1.0Al–0.6Ce glass. This result demonstrated that the introduction of CeF_3 as a sensitizer successfully established an efficient ET channel from Ce^{3+} to Tb^{3+}. The XEL intensity of GL–6Tb–1.0Al–0.6Ce is greater than that of most Tb^{3+}-doped glass scintillators and glass-ceramic (GC) scintillators (Table 1).

The long-term irradiation hardness values of GL–6Tb–1.0Al–0.6Ce and GL–6Tb were investigated and are compared in Fig. 3(d). During the first 50 min of irradiation, the XEL intensities of GL–6Tb–1.0Al–0.6Ce and GL–6Tb continue to increase because of the "bright burn effect". The luminescent centers compete with the traps in the process of capturing electrons. As the irradiation time increases, traps are gradually filled. The electrons are completely captured by the luminescent centers, which leads to an increase in the XEL intensity. After

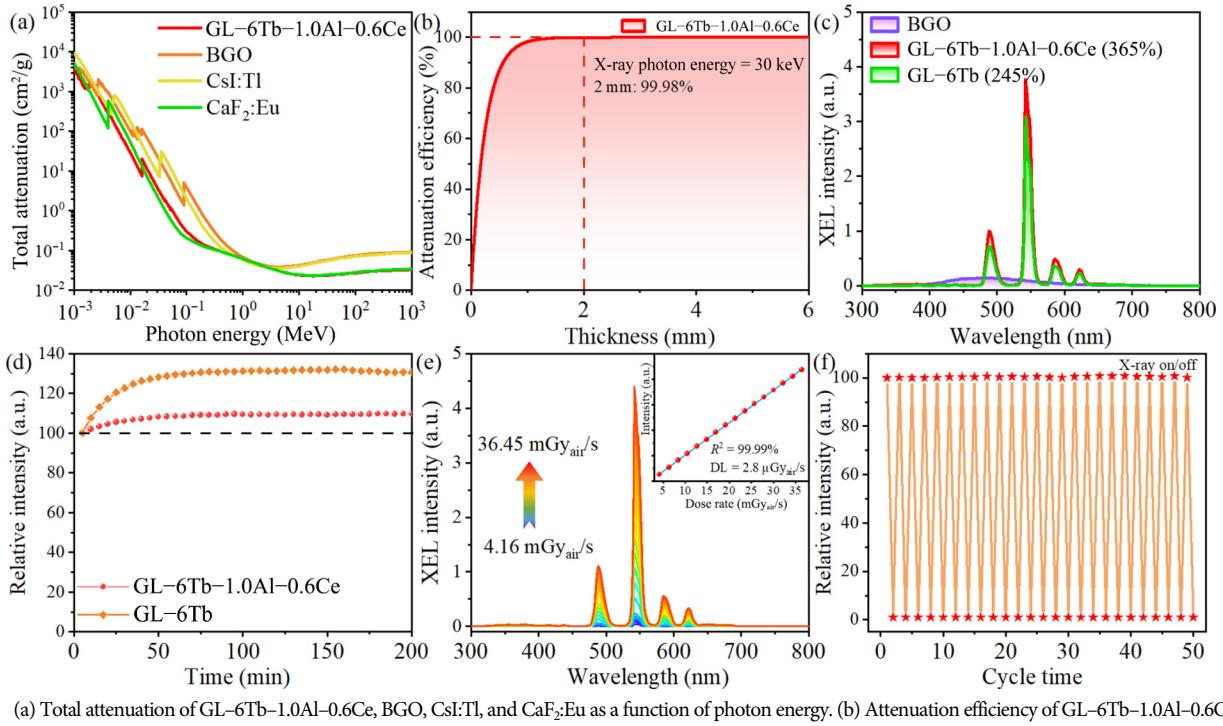

Fig. 3 (a) Total attenuation of GL–6Tb–1.0Al–0.6Ce, BGO, CsI:Tl, and CaF_2:Eu as a function of photon energy. (b) Attenuation efficiency of GL–6Tb–1.0Al–0.6Ce as a function of thickness. (c) XEL spectra of BGO, GL–6Tb, and GL–6Tb–1.0Al–0.6Ce. (d) Relative intensity of GL–6Tb–1.0Al–0.6Ce and GL–6Tb as a function of irradiation time. (e) Dose rate-dependent XEL spectra of GL–6Tb–1.0Al–0.6Ce. (f) X-ray switching cycles for 50 cycles.

50 min of irradiation, the XEL intensity of GL–6Tb–1.0Al–0.6Ce increased by 1.10 times, whereas the XEL intensity of GL–6Tb increased by 1.30 times. This indicates that the GL–6Tb–1.0Al–0.6Ce glass scintillator has better irradiation stability than does GL–6Tb. In addition, after 200 min of irradiation, the decrease in the transmittance of the GL–6Tb glass was more obvious than that of the GL–6Tb–1.0Al–0.6Ce glass (Fig. S12 in the ESM). This further illustrates that the GL–6Tb–1.0Al–0.6Ce glass scintillator has better irradiation stability under prolonged X-ray irradiation. In addition, the irradiation-induced damage to GL–6Tb–1.0Al–0.6Ce and GLv6Tb could be repaired after heat treatment at 400 °C for 4 h (Fig. S12 in the ESM). The transmittance of glass decreases because of the capture of electrons by traps and the formation of color centers, which can absorb wavelengths of visible light and decrease the transmittance [47]. After heat treatment, the captured electrons are released, and the color centers vanish [48]. Therefore, the transmittance and XEL intensity of GL–6Tb–1.0Al–0.6Ce are restored (Fig. S12 in the ESM). The increase in irradiation hardness is due to ionic valence conversion. X-rays can promote the valence transformation of Ce^{4+} to Ce^{3+}. Ce^{4+} acts as an "electron absorption trap" and reduces the binding of carriers to defects. Therefore, the number of electrons captured by traps is lower in GL–6Tb–1.0Al–0.6Ce than in GL–6Tb, which improves the irradiance performance [49].

Figure 3(e) displays the XEL spectra at different dose rates. With increasing dose rates, the XEL intensity of GL–6Tb–1.0Al–0.6Ce increases. As shown in the inset of Fig. 3(e), the GL–6Tb–1.0Al–0.6Ce glass scintillator demonstrates an outstanding linear response to X-ray dose rates over a wide range from 4.16 to 36.45 mGy_{air}/s, and the correlation coefficient can reach 99.99%, which is conducive to obtaining X-ray imaging with high imaging contrast. GL–6Tb–1.0Al–0.6Ce has the lowest detection limit of 2.8 $\mu Gy_{air}/s$, which is significantly below the standard diagnostic threshold of 5.5 $\mu Gy_{air}/s$.

The repeatability of GL–6Tb–1.0Al–0.6Ce was verified through X-ray cycling tests, as shown in Fig. 3(f). After 50 cycles of X-ray on-off irradiation, there was no significant decrease in the XEL intensity of GL–6Tb–1.0Al–0.6Ce, which illustrates that GL–6Tb–1.0Al–0.6Ce displays high stability under repeated X-ray irradiation.

3.4 Thermal stability of GL–6Tb–1.0Al–0.6Ce in XEL

The thermal stability of GL–6Tb–1.0Al–0.6Ce in XEL was examined in Fig. 4. The temperature-dependent XEL spectra of GL–6Tb–1.0Al–0.6Ce are shown in Fig. 4(a) and Fig. S13 in the ESM. Anti-thermal-quenching behavior could be observed in GL–6Tb–1.0Al–0.6Ce. The XEL intensity of GL–6Tb–1.0Al–0.6Ce increases with increasing temperature. As shown in Fig. 4(b), at 573 K, the XEL intensity of GL–6Tb–1.0Al–0.6Ce is 168% of that at 303 K. In addition, anti-thermal-quenching behavior can also be observed in GL–6Tb. As the temperature increased, the XEL intensity of GL–6Tb increased. At 573 K, the XEL intensity of GL–6Tb is 128% of that at 303 K. However, the XEL intensity of GL–1.0Al–0.6Ce decreases with increasing temperature. At 573 K, the XEL intensity of GL–1.0Al–0.6Ce is 74% of that at room temperature. In addition, the XEL intensities of CsI:Tl and BGO decrease more strongly with increasing temperature. At 573 K, the XEL intensities of BGO and CsI:Tl are only 1% of those at 303 K. As listed in Table S6 in the ESM, thermal quenching is more common in most scintillators. In contrast, GL–6Tb–1.0Al–0.6Ce exhibits anti-thermal-quenching performance, which illustrates that GL–6Tb–1.0Al–0.6Ce possesses the best thermal stability.

The anti-thermal-quenching phenomenon under X-ray irradiation is attributed to the establishment of dual-channel thermally enhanced ET, including a thermal compensation effect from traps to Tb^{3+} and thermally enhanced ET from Ce^{3+} to Tb^{3+}. GL–6Tb exhibits anti-thermal-quenching luminescence, which could be attributed to the thermal compensation effect from intrinsic traps. As shown by the thermoluminescence (TL) spectra in Fig. S14(a) in the ESM, these traps store electrons during X-ray irradiation and release electrons upon heating, partially offsetting thermal quenching losses (the XEL intensity at 573 K is 128% of that at room temperature). Remarkably, the codoping of CeF_3 in GL–6Tb–1.0Al–0.6Ce significantly enhances this anti-thermal-quenching luminescence, with the XEL intensity at 573 K peaking at an impressive 168% of its room-temperature value. This superior performance is attributed to a dual-channel thermally enhanced ET mechanism. The first channel is thermally enhanced ET from the sensitizer Ce^{3+} to the activator Tb^{3+}, which is confirmed by the PL spectra. The second channel is the thermal compensation effect from traps to Tb^{3+}. A direct comparison of the TL spectra reveals that the TL intensity of GL–6Tb–1.0Al–0.6Ce (Fig. S14(b) in the ESM) is much greater than that of GL–6Tb, indicating a substantial increase in trap density due to Ce^{3+} codoping. At elevated temperatures, these traps provide more powerful and sustained release of stored electrons to Tb^{3+}, creating a highly effective compensation channel. Therefore, the synergistic combination of thermally enhanced ET from Ce^{3+} to Tb^{3+} and the Ce^{3+}-induced increase in trap-mediated thermal compensation

Table 1 I_{XEL} of Tb^{3+}-doped glass and GC scintillators

Sample	I_{XEL}	Resolution (lp/mm)	Ref.
BGO	100%	—	—
B_2O_3–GeO_2–TeO_2–Gd_2O_3:Tb^{3+} glass	9.1%	—	[38]
SiO_2–B_2O_3–Al_2O_3–Gd_2O_3:Tb^{3+} glass	40%	—	[39]
CaF_2:Tb^{3+} GC	50%	—	[40]
SiO_2–AlF_3–Al_2O_3–Gd_2O_3:Ce^{3+}/Tb^{3+}	67%	10	[41]
$BaGdF_5$:Tb^{3+} GC	140%	—	[42]
Sr_2GdF_7:Tb^{3+} GC	194%	—	[43]
SiO_2–Li_2O–Al_2O_3–NaF–GdF_3:Tb^{3+}	209%	30	[32]
SiO_2–Al_2O_3–BaF_2–NaF:Tb^{3+}	224%	20	[44]
SiO_2–B_2O_3–Na_2CO_3–BaF_2–GdF_3:Tb^{3+}	250%	20	[45]
SiO_2–Al_2O_3–SrF_2–NaF:Tb^{3+}	350%	24	[46]
GL–6Tb–1.0Al–0.6Ce	365%	24	This work

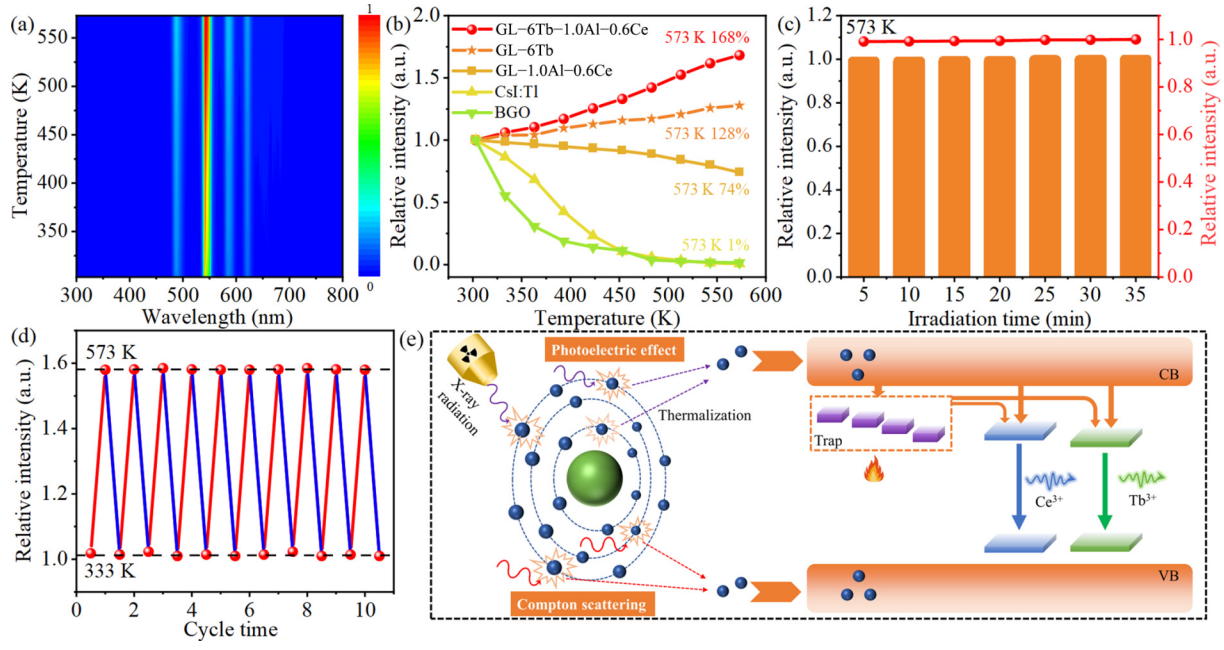

Fig. 4 (a) Contour plot of temperature-dependent XEL spectra of GL–6Tb–1.0Al–0.6Ce. (b) Relative XEL intensity of GL–6Tb–1.0Al–0.6Ce, G–6Tb, G–0.6Ce–1.0Al, CsI:Tl, and BGO as a function of temperature. (c) Relative integrated XEL intensity with respect to irradiation time. (d) Repeatability (303 and 573 K) of GL–6Tb–1.0Al–0.6Ce. (e) XEL mechanism.

substantially improved the thermal stability of GL–6Tb–1.0Al–0.6Ce over that of GL–6Tb. This dual-channel enhancement strategy presents a promising avenue for designing materials for high-temperature X-ray imaging applications.

Figure 4(c) shows the thermal stability of the XEL of GL–6Tb–1.0Al–0.6Ce at 573 K under long-term irradiation. During 35 min of X-ray irradiation, the XEL intensity of GL–6Tb–1.0Al–0.6Ce at 573 K remained stable. Figure 4(d) shows the temperature cycling performance of GL–6Tb–1.0Al–0.6Ce. After ten temperature cycles, the fluctuation in the XEL intensity of GL–6Tb–1.0Al–0.6Ce was negligible. These results demonstrate that GL–6Tb–1.0Al–0.6Ce has excellent thermal stability under long-term irradiation.

Figure 4(e) illustrates the XEL and anti-thermal-quenching mechanisms in the GL–6Tb–1.0Al–0.6Ce glass scintillators. Upon irradiation, incident X-ray photons are absorbed by the glass, producing primary high-energy electrons through the photoelectric effect and Compton scattering. These energetic electrons generate a multitude of secondary electrons and holes via impact ionization. These electrons and holes subsequently rapidly thermalize to the valence band (VB) and conduction band (CB) edges and migrate to the lattice. During migration, carriers are captured by luminescent centers (Ce^{3+} and Tb^{3+}) and traps. When the temperature increases gradually, the electrons captured by traps are released under thermal activation, and these electrons are subsequently transported to Ce^{3+} and Tb^{3+}. ET from traps to Tb^{3+} compensates for the thermal quenching of Tb^{3+} [50–53]. In addition, by absorbing the energy of secondary electrons, Ce^{3+} and Tb^{3+} are excited to the excited state. For Ce^{3+}, the electrons in the 5d excited state radiatively relax to the 4f ground state and emit light. Some of the electrons of Ce^{3+} transfer energy to Tb^{3+}, and the electrons of Tb^{3+} are excited to the excited state. For Tb^{3+}, the electrons nonradiatively relax from the excited state, and then, the electrons transition back to the ground state, producing green luminescence.

The excellent anti-thermal-quenching performance of GL–6Tb–1.0Al–0.6Ce is attributed to two synergistic, thermally enhanced ET pathways that supply energy to Tb^{3+}. The first pathway is thermally enhanced ET from Ce^{3+} sensitizers to Tb^{3+} activators. As the temperature increases, the ET efficiency increases. The second pathway involves the thermal compensation effect. As the temperature increases, the electrons captured by traps become thermally activated and delocalize, migrating through the CB to the excited states of the luminescent centers. The resulting emission from these additionally activated electrons compensates for the nonradiative transitions at high temperature.

In summary, dual-channel tharmal-enhanced ET, including thermally enhanced ET from Ce^{3+} to Tb^{3+} and a thermal compensation effect from traps to Tb^{3+}, led to the superior anti-thermal-quenching performance of GL–6Tb–1.0Al–0.6Ce.

3.5 X-ray imaging application

X-ray imaging applications of GL–6Tb–1.0Al–0.6Ce (1 mm) at room temperature, at high temperature, and underwater were investigated via a custom-made X-ray instrument and are shown in Fig. 5. Figure 5(a) shows a schematic diagram of the X-ray imaging instrument. When an X-ray passes through an imaging object, the X-ray carries information about the internal structure of the imaging object. Subsequently, the glass scintillators efficiently convert X-rays into visible light. The visible light is reflected by the mirror and received by a camera. Ultimately, a clear X-ray image of the internal structure of the object is obtained.

Various objects, including ballpoint pens, peanuts and chips, are imaged under daylight and X-ray irradiation, as shown in Fig. 5(b). The changes in the ballpoint pen tip and spring can be clearly observed. Two peanuts inside the peanut shell and the circuits in the chip are both clearly visible. There are no ghost images in X-ray imaging. Therefore, GL–6Tb–1.0Al–0.6Ce glass scintillators with millisecond lifetimes are suitable for static X-ray imaging. A standard line pair card was used to characterize the X-ray imaging ability of GL–6Tb–1.0Al–0.6Ce. The spatial resolution of GL–6Tb–1.0Al–0.6Ce reaches 24 lp/mm, as shown in Fig. 5(c) and Fig. S15 in the ESM. The modulation transfer function (MTF) was employed to further quantify the spatial

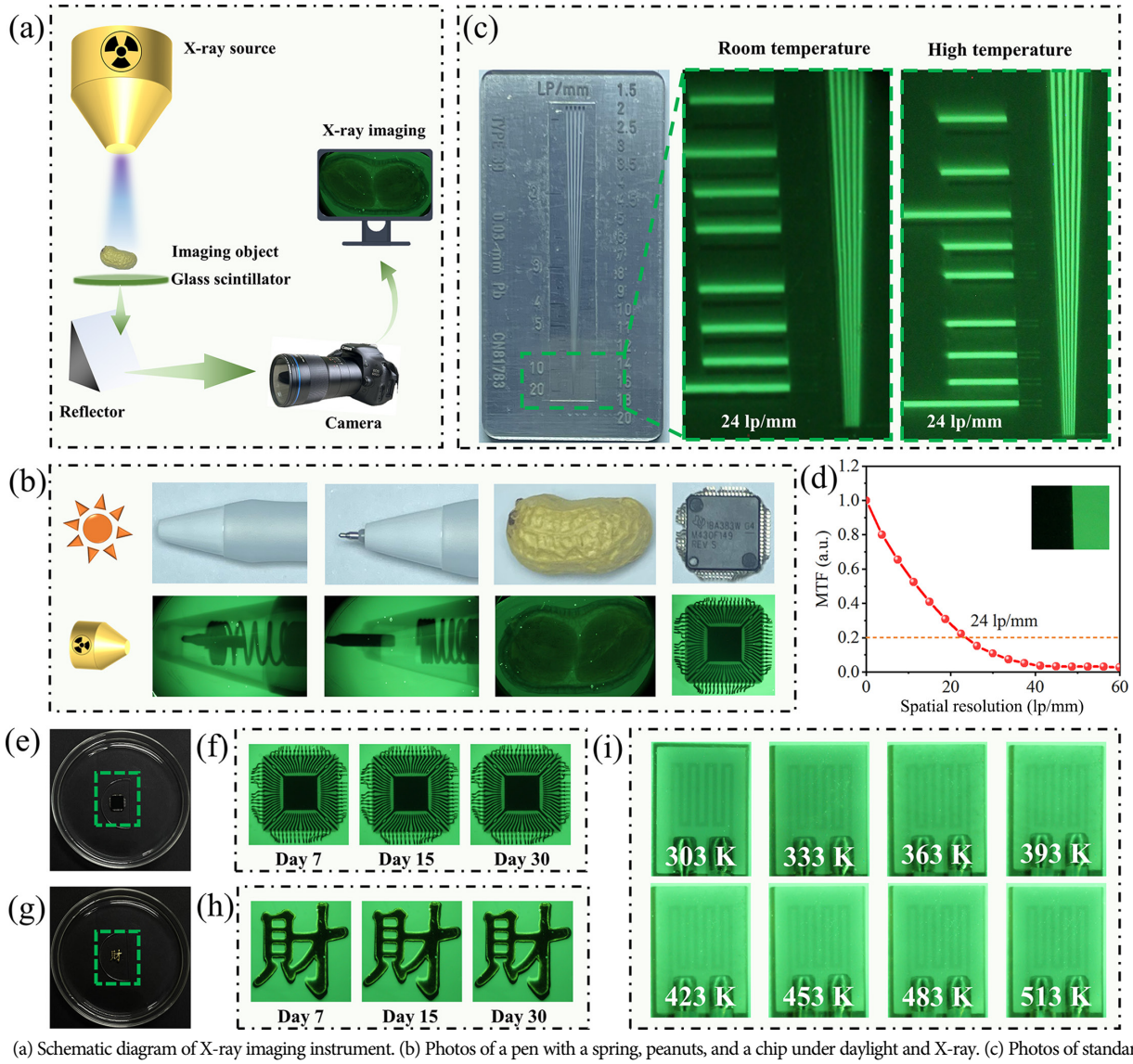

Fig. 5 (a) Schematic diagram of X-ray imaging instrument. (b) Photos of a pen with a spring, peanuts, and a chip under daylight and X-ray. (c) Photos of standard line pair card for daylight and X-ray imaging, as well as photos under X-ray at room temperature (left) and high-temperature (right) conditions. (d) MTF spectra as a function of spatial resolution. (e) Schematic diagram of a chip immersed in water. (f) X-ray images of chip immersed in water for 7, 15, and 30 days. (g) Schematic diagram of a Chinese character immersed in water. (h) X-ray images of Chinese characters immersed in water for 7, 15, and 30 days. (i) X-ray images of a heated ceramic plate ranging from 303–513 K.

resolution of GL–6Tb–1.0Al–0.6Ce. As shown in Fig. 5(d), the spatial resolution of the GL–6Tb–1.0Al–0.6Ce scintillator determined from the MTF is 24 lp/mm when the MTF is 0.2.

Figures 5(e) and 5(f) show underwater photographs of a chip under daylight and X-ray irradiation, respectively. Under X-ray irradiation, the circuits in the chip are still clearly visible under water. Figures 5(g) and 5(h) display underwater photographs of a Chinese character metal pattern under daylight and X-ray irradiation, respectively. With increasing immersion time, the brightness and clarity of the metal pattern and the chip remain unchanged. These results prove the physicochemical stability of GL–6Tb–1.0Al–0.6Ce in water and that GL–6Tb–1.0Al–0.6Ce has potential application in underwater X-ray imaging.

GL–6Tb–1.0Al–0.6Ce possesses excellent XEL thermal stability. Therefore, GL–6Tb–1.0Al–0.6Ce could be applied in high-temperature X-ray imaging. As shown in Fig. 5(i), the brightness of the X-ray images of the heated plates increases with increasing temperature (Fig. S16 in the ESM). The high-temperature X-ray imaging ability of GL–6Tb–1.0Al–0.6Ce was estimated, as shown in Fig. 5(c). The spatial resolution at 363 K remains 24 lp/mm. Therefore, GL–6Tb–1.0Al–0.6Ce has potential for X-ray imaging at high temperatures.

4 Conclusions

In this study, Tb^{3+}-doped glass scintillators with outstanding luminescent efficiency and remarkable thermal stability were designed and developed. For PL, the GL–6Tb–1.0Al–0.6Ce glass scintillators present a high IQE (85.3%) and excellent PL thermal stability (90.2% at 573 K). For XEL, record-breaking XEL intensity (365% of that of BGO), a low detection limit (2.8 $\mu Gy_{air}/s$), and good irradiation hardness are obtained. By codoping Ce^{3+}, a dual-channel thermally enhanced ET strategy is realized, including thermally enhanced ET from Ce^{3+} to Tb^{3+} and a thermal compensation effect from traps to Tb^{3+} with increasing density of traps. As a result, the most significant finding, profound anti-thermal-quenching behavior with XEL intensity at 573 K reaching 168% of that at 303 K, is achieved. This superior thermal performance enables high-resolution X-ray imaging (up to 24 lp/mm) at both room temperature and high temperature.

These collective results confirm that GL–6Tb–1.0Al–0.6Ce glass is a highly promising candidate for demanding applications, such as high-temperature nondestructive testing. The elucidated dual-channel thermally enhanced ET strategy offers clear and effective guidance for the future design of scintillators with superior thermal stability.

Acknowledgements

This work was supported by the National Natural Science Foundation of China (Nos. 1254443 and 52372016).

Author contributions

Lianjie Li: Investigation, Writing—original draft; Junyu Chen: Methodology, Writing—original draft; Guanlin He: Investigation, Writing—original draft; Xvsheng Qiao: Methodology, Resources, Writing—review & editing; Hai Guo: Conceptualization, Resources, Writing—review & editing, supervision.

Availability of data and materials

The data that support the findings of this study are available from the corresponding author upon reasonable request.

Competing interests

The authors have no competing interests to declare that are relevant to the content of this article.

Electronic Supplementary Material

Supplementary material is available in the online version of this article at https://doi.org/10.26599/JAC.2025.9221220.

References

[1] Chen QS, Wu J, Ou XY, *et al.* All-inorganic perovskite nanocrystal scintillators. *Nature* 2018, **561**: 88–93.

[2] Shao WY, He TY, Wang LJ, *et al.* Capillary manganese halide needle-like array scintillator with isolated light crosstalk for micro-X-ray imaging. *Adv Mater* 2024, **36**: 2312053.

[3] Kim YC, Kim KH, Son DY, *et al.* Printable organometallic perovskite enables large-area, low-dose X-ray imaging. *Nature* 2017, **550**: 87–91.

[4] Li HJ, Dong QH, Li Y, *et al.* Thermal-adaptive photonic MOFs for high-performance X-ray scintillator. *Adv Funct Mater* 2025, **35**: 2500445.

[5] Wang T, Hu S, Ji T, *et al.* High-temperature X-ray imaging with transparent ceramics scintillators. *Laser Photonics Rev* 2024, **18**: 2300892.

[6] Wang TC, Yao SY, Yan SP, *et al.* High thermal stability of copper-based perovskite scintillators for high-temperature X-ray detection. *ACS Appl Mater Inter* 2023, **15**: 23421–23428.

[7] Kim C, Lee W, Melis A, *et al.* A review of inorganic scintillation crystals for extreme environments. *Crystals* 2021, **11**: 669.

[8] Zou YC, Xiang SK, Dai CD. Spontaneous formation of filled-shell CsI-Xenon solid solutions under high temperature and high pressure. *Comp Mater Sci* 2021, **192**: 110355.

[9] Moncorgé R, Jacquier B, Boulon G. Temperature dependent luminescence of $Bi_4Ge_3O_{12}$ discussion on possible models. *J Lumin* 1976, **14**: 337–348.

[10] Kastengren A. Thermal behavior of single-crystal scintillators for high-speed X-ray imaging. *J Synchrotron Radiat* 2019, **26**: 205–214.

[11] Liu JQ, Zhao XD, Xu YS, *et al.* All-inorganic glass scintillators: Scintillation mechanism, materials, and applications. *Laser Photonics Rev* 2023, **17**: 2300006.

[12] Wang SK, Yang JD, Liu C, *et al.* $KTb_{3-x}Gd_xF_{10}$ nano-glass composite scintillator with excellent thermal stability and record X-ray imaging resolution. *Laser Photonics Rev* 2025, **19**: 2401611.

[13] Wang DZ, Li HW, Chen JF, *et al.* Congruent glass composite scintillator for efficient high-energy ray detection. *Adv Mater* 2025, **37**: 2412661.

[14] He GL, Chen JY, Li LJ, *et al.* Cu^+-doped oxyfluoride glass with anti-thermal-quenching luminescence for X-ray imaging and WLED. *J Adv Ceram* 2025, **14**: 9221116.

[15] He GL, Li LJ, Chen JY, *et al.* A thermal stable multi-functional Cu^+-doped glass for high-resolution X-ray imaging and full-spectra lighting. *Laser Photonics Rev* 2025, **19**: 00396.

[16] Li LJ, Chen JY, He GL, *et al.* High transparent $Sr_{0.84}Tb_{0.16}F_{2.16}$ glass-ceramic scintillators with excellent thermal stability for high-temperature X-ray imaging. *Adv Opt Mater* 2025, **13**: 01331.

[17] Wang YZ, Jing W, Li WW, *et al.* Preparation of $(Tb_{0.94-x}Lu_{0.06}Ho_x)_2O_3$ transparent ceramics with high Verdet constants for magneto-optical applications. *J Adv Ceram* 2025, **14**: 9221035.

[18] Pang T, Lin SS, You FL, *et al.* Synergistic enhancement of crystallinity and transparency in Tb^{3+}-doped nano-glass-ceramics for high-resolution X-ray imaging. *J Adv Ceram* 2025, **14**: 9221122.

[19] Qin X, Liu XW, Huang W, *et al.* Lanthanide-activated phosphors based on 4f-5d optical transitions: Theoretical and experimental aspects. *Chem Rev* 2017, **117**: 4488–4527.

[20] Wu QS, Zhou XF, Ye SS, *et al.* Visual ratiometric optical thermometer with high sensitivity and excellent signal discriminability based on $LiScSiO_4$: Ce^{3+}, Tb^{3+} thermochromic phosphor. *Spectrochim Acta A-M* 2023, **294**: 122534.

[21] Zhang XG, Huang YM, Gong ML. Dual-emitting Ce^{3+}, Tb^{3+} co-doped LaOBr phosphor: Luminescence, energy transfer and ratiometric temperature sensing. *Chem Eng J* 2017, **307**: 291–299.

[22] Ding MY, Lu CH, Chen L, *et al.* Ce^{3+}/Tb^{3+} co-doped β-$NaYF_4$ dual-emitting phosphors for self-referencing optical thermometry. *J Alloys Compd* 2018, **763**: 85–93.

[23] Li L, Diao YF, Liu X. Ce–Mn mixed oxides supported on glass-fiber for low-temperature selective catalytic reduction of NO with NH_3. *J Rare Earth* 2014, **32**: 409–415.

[24] Huang RY, Zhang X, Xu XM, *et al.* Double perovskite scintillators enabled by Co-doped trap regulation for thermally enhanced X-ray imaging. *Adv Opt Mater* 2025, **13**: 2403289.

[25] Du J, Cormack AN. The medium range structure of sodium silicate glasses: A molecular dynamics simulation. *J Non Cryst Solids* 2004, **349**: 66–79.

[26] Cormack AN, Du J, Zeitler TR. Alkali ion migration mechanisms in silicate glasses probed by molecular dynamics simulations. *Phys Chem Chem Phys* 2002, **4**: 3193–3197.

[27] Liu QH, Ran P, Chen WL, *et al.* Bright transparent scintillators with high fraction $BaCl_2$: Eu^{2+} nanocrystals precipitation: An ionic-covalent hybrid network strategy toward superior X-ray imaging glass-ceramics. *Adv Sci* 2023, **10**: 2304889.

[28] Chen S, Zhang WN, Teng LM, *et al.* Design, simulation, elaboration and luminescence of Tb^{3+}-doped $Ba_{0.84}Gd_{0.16}F_{2.16}$ fluoroaluminosilicate scintillating glass ceramics. *J Eur Ceram Soc* 2021, **41**: 6722–6728.

[29] Zhao JJ, Xu XX, Chen XT, *et al.* A structure model for phase separated fluoroaluminosilicate glass system by molecular dynamic simulations. *J Eur Ceram Soc* 2019, **39**: 5018–5029.

[30] Xu XX, Zhao JJ, Chen XT, *et al.* $Ca^{2+}/Sr^{2+}/Ba^{2+}$ dependent phase separation, nanocrystallization and photoluminescence in fluoroaluminosilicate glass. *J Am Ceram Soc* 2020, **103**: 5796–5807.

[31] Zhao JJ, Xu XX, Li PC, *et al.* Structural origins of $RF_3/NaRF_4$ nanocrystal precipitation from phase-separated SiO_2–Al_2O_3–RF_3–NaF glasses: A molecular dynamics simulation study. *J Phys Chem B* 2019, **123**: 3024–3032.

[32] Zhang DD, Lin SS, Xia ML, *et al.* Flexibly prepared Tb^{3+}-doped oxyfluoride glass scintillators with enhanced luminescence for X-ray imaging and detection. *Laser Photonics Rev* 2025, **19**: 2500354.

[33] Wilmarth WR, Begun GM, Nave SE, *et al.* The Raman spectra of polycrystalline orthorhombic YF_3, SmF_3, HoF_3, YbF_3, and single crystal TbF_3. *J Chem Phys* 1988, **89**: 711–715.

[34] Le Parc R, Champagnon B, Dianoux J, *et al.* Anorthite and

$CaAl_2Si_2O_8$ glass: Low frequency Raman spectroscopy and neutron scattering. *J Non Cryst Solids* 2003, **323**: 155–161.
[35] Wu MC, Yu MD, Cheng X, *et al.* Energy transfer study on dense and transparent Eu^{3+}/Tb^{3+}-coactivated TeO_2–Gd_2O_3–WO_3–ZnO glass scintillators. *J Rare Earth* 2025, **43**: 1364–1372.
[36] Zhang F, Wang DZ, Du GX, *et al.* Superdense Ce^{3+}-activated lutetium silicate scintillating glass for radiation detection. *J Rare Earth* 2025, **43**: 2137–2144.
[37] Guo JJ, Li LJ, Chen JY, *et al.* Ce^{3+}-doped oxyfluoride glass scintillator: Optimized radioluminescence and application in X-ray imaging. *J Alloys Compd* 2024, **980**: 173670.
[38] Han TT, Sun XY, Lai XQ, *et al.* Role of Gd_2O_3 on tailoring structural and optical properties of Tb^{3+}-activated borogermanate-tellurite glasses. *Radiat Phys Chem* 2021, **189**: 109734.
[39] Chewpraditkul W, Sheng QC, Chen DP, *et al.* Luminescence of Tb^{3+}-doped oxide glasses with high Gd_2O_3 concentration under UV and X-ray excitation. *Phys Status Solidi A* 2012, **209**: 2578–2582.
[40] Zhao JT, Huang LH, Zhao SL, *et al.* Enhanced luminescence in Tb^{3+}-doped germanate glass ceramic scintillators containing CaF_2 nanocrystals. *J Am Ceram Soc* 2019, **102**: 1720–1725.
[41] Wu YH, Chen DY, Li Y, *et al.* Scintillation properties of Ce^{3+}/Tb^{3+} co-doped oxyfluoride aluminosilicate glass for exploration of X-ray imaging. *J Lumin* 2022, **245**: 118762.
[42] Zheng ZG, Tong Y, Wei RF, *et al.* Tb^{3+}-doped transparent $BaGdF_5$ glass-ceramics scintillator for X-ray detector. *J Am Ceram Soc* 2020, **103**: 2548–2554.
[43] Teng LM, Zhang WN, Chen WP, *et al.* Highly efficient luminescence in bulk transparent Sr_2GdF_7: Tb^{3+} glass ceramic for potential X-ray detection. *Ceram Int* 2020, **46**: 10718–10722.
[44] Li LJ, Chen JY, Wen ZX, *et al.* X-ray imaging scintillator: Tb^{3+}-doped oxyfluoride aluminosilicate glass. *Ceram Int* 2024, **50**: 757–763.
[45] Li LJ, Chen JY, Peng XS, *et al.* High-resolution Tb^{3+}-doped Gd-based oxyfluoride glass scintillators for X-ray imaging. *J Mater Chem C* 2023, **11**: 11664–11670.
[46] Li LJ, Chen JY, He GL, *et al.* Anti-thermal-quenching radioluminescence and high-temperature X-ray imaging of Tb^{3+} doped glass scintillators. *Sci China Mater* 2025, **68**: 1–11.
[47] Gao S, Duan YZ, Tian ZN, *et al.* Laser-induced color centers in crystals. *Opt Laser Technol* 2022, **146**: 107527.
[48] Bai X, Zhang YT, Zhao HP, *et al.* Flexible X-ray detector for cumulative dose monitoring through reversible photochromism and luminescence modulation. *Adv Sci* 2025, **12**: 2412986.
[49] Tang YM, Deng MX, Liu QN, *et al.* Reducing luminescence intensity and suppressing irradiation-induced darkening of $Bi_4Ge_3O_{12}$ by Ce-doping for radiation detection. *Adv Opt Mater* 2024, **12**: 2301332.
[50] Xu WX, Zhang SN, Wei AQ, *et al.* Advancing multi-optical performances in lanthanide-doped fluoride core@shell nanoarchitectures by minimizing cation intermixing. *Adv Funct Mater* 2025, **35**: 2415815.
[51] Zou HR, Zhu WJ, Zhao JT, *et al.* Sub-10 nm lanthanide-doped $Lu_6O_5F_8$ nanoscintillators for real-time high-resolution dynamic 3D X-ray imaging. *Adv Funct Mater* 2024, **34**: 2409156.
[52] Lei L, Yi MH, Wang YB, *et al.* Dual heterogeneous interfaces enhance X-ray excited persistent luminescence for low-dose 3D imaging. *Nat Commun* 2024, **15**: 1140.
[53] Lei L, Wang YB, Xu WX, *et al.* Manipulation of time-dependent multicolour evolution of X-ray excited afterglow in lanthanide-doped fluoride nanoparticles. *Nat Commun* 2022, **13**: 5739.